Published in final edited form as:

Proc SPIE Int Soc Opt Eng. 2018 February ; 10574: . doi:10.1117/12.2293790.

Inter-scanner Variation Independent Descriptors for Constrained Diffeomorphic Demons Registration of Retina OCT

S. Reaungamornrat[a], **A. Carass**[a], **Y. He**[a], **S. Saidha**[b], **P.A. Calabresi**[b], **J. L. Prince**[a]

[a]Department of Neurology, Johns Hopkins Hospital, Baltimore, MD

[b]Department of Electrical and Computer Engineering, Johns Hopkins University, Baltimore MD

Abstract

Purpose—OCT offers high in-plane micrometer resolution, enabling studies of neurodegenerative and ocular-disease mechanisms via imaging of the retina at low cost. An important component to such studies is inter-scanner deformable image registration. Image quality of OCT, however, is suboptimal with poor signal-to-noise ratio and through-plane resolution. Geometry of OCT is additionally improperly defined. We developed a diffeomorphic deformable registration method incorporating constraints accommodating the improper geometry and a decentralized-modality-insensitive-neighborhood-descriptors (D-MIND) robust against degradation of OCT image quality and inter-scanner variability.

Method—The method, called D-MIND Demons, estimates diffeomorphisms using D-MINDs under constraints on the direction of velocity fields in a MIND-Demons framework. Descriptiveness of D-MINDs with/without denoising was ranked against four other shape/texture-based descriptors. Performance of D-MIND Demons and its variants incorporating other descriptors was compared for cross-scanner, intra- and inter-subject deformable registration using clinical retina OCT data.

Result—D-MINDs outperformed other descriptors with the difference in mutual descriptiveness between high-contrast and homogenous regions > 0.2. Among Demons variants, D-MIND-Demons was computationally efficient, demonstrating robustness against OCT image degradation (noise, speckle, intensity-non-uniformity, and poor through-plane resolution) and consistent registration accuracy [(4±4 μm) and (4±6 μm) in cross-scanner intra- and inter-subject registration] regardless of denoising.

Conclusions—A promising method for cross-scanner, intra- and inter-subject OCT image registration has been developed for ophthalmological and neurological studies of retinal structures. The approach could assist image segmentation, evaluation of longitudinal disease progression, and patient population analysis, which in turn, facilitate diagnosis and patient-specific treatment.

Keywords

deformable image registration; Demons algorithm; diffeomorphism; descriptors; optical coherence tomography; OCT

1. INTRODUCTION

Optical coherence tomography (OCT) offers low-cost microscopic imaging of the retina, therefore facilitating detection and study of various neurological disorders, including multiple sclerosis[1] and Alzheimer's disease.[2] Registration of OCT acquired using different imaging systems, particularly from different vendors, facilitates the longitudinal study of disease progression, population analysis, and segmentation, which, in turn, benefit diagnosis and precision medicine treatment. In this work, D-MIND Demons was developed based on MIND Demons[3] to enable cross-scanner, inter-subject diffeomorphic deformable registration of 3D OCT images. The method improves insensitivity to image quality and differences in image characteristics of OCT by incorporating a decentralized modality insensitive neighborhood descriptors (D-MIND) combining a Huber metric and an asymmetric stencil to accommodate noise, speckle, and strongly anisotropic and dissimilar voxel size of cross-scanner OCT images. As OCT does not reflect the physical geometry of image acquisition,[4] the method constrains velocity fields of diffeomorphisms to be parallel to the A-scan direction. The registration method and D-MINDs are described in Section 2. Since OCT exhibits poor signal-to-noise ratio,[4] the effects of denoising methods [i.e., block-matching and 3D (BM3D) filtering[5] and foveated nonlocal means (FNLM) filtering[6]] on the ability of descriptors to encode local structure and/or texture in images are presented in Sections 3 and 4. The sections additionally demonstrate the performance of the D-MIND Demons method in cross-scanner intra- and inter-subject registration using clinical OCT data compared to its variants—i.e., integrating D-MINDs with other descriptors including average image gradients (AG), compact histograms of image orientation (CHO), co-occurrence (COC) texture features,[7] and run length (RL) texture features[8]. Advantages and limitations as well as future work are discussed in Section 5.

2. METHODS

2.1. Image Descriptors

Intensity non-uniformity, noise, speckle, and thick through-plane resolution (slice-separation) of OCT images challenge intensity-based deformable registration. Instead of using a robust metric which could involve complex calculations,[9–11] we consider image descriptors which provide a rich encoding of local structural and/or texture while reducing the effect of image degradation to registration performance. The section describes the D-MIND, AG, and CHO descriptors.

1. Decentralized-modality-insensitive neighborhood descriptor (D-MIND)—

D-MINDs are robust to intensity inhomogeneity and invariant to imaging modalities, thus insensitive to global intensity change between distinct scanners. D-MINDs improve upon MINDs[3,12] to accommodate OCT image quality. Calculation of descriptor elements involves a stencil $\mathcal{N}_s$ and a patch $\mathcal{N}_p$ which is decentralized such that patch distances are computed between patches of points $\boldsymbol{r}_j, \boldsymbol{r}_k \in \mathcal{N}_s$ for indices $j, k \in \{1,2,3, \ldots ,10\}$ and $j \neq k$ [Figs. 1(a,b)]—instead of between patches of points $\boldsymbol{r}_j \in \mathcal{N}_s$ and the patch of the center point $\boldsymbol{x}$ of $\mathcal{N}_s$, denoted *center patch*—to reduce the influence of the degradation of the center patch to the performance of descriptors. Each i-th element $d_{I,i}(\boldsymbol{x})$ of a D-MIND $\boldsymbol{d}_I(\boldsymbol{x}) \in \mathbb{R}^D$ in an image I is therefore

$$d_{I,i}(\boldsymbol{x}) = c \exp\left(-\frac{H_{\mathcal{N}_p}\left(I, \boldsymbol{r}_j, \boldsymbol{r}_k\right)}{V(I, \boldsymbol{x})}\right), \tag{1}$$

where c is a normalization factor and $V(I, \boldsymbol{x})$ is the local variance. The patch distance $H_{\mathcal{N}_p}$ is computed using a Huber metric[13] H to improve robustness against noise and speckle as

$$H_{\mathcal{N}_p}\left(I, \boldsymbol{r}_j, \boldsymbol{r}_k\right) = \frac{1}{\left|\mathcal{N}_p\right|} \sum_{z \in \mathcal{N}_p} H\left(I\left(\boldsymbol{r}_j + z\right), I\left(\boldsymbol{r}_k + z\right)\right), \tag{2}$$

where $\boldsymbol{z}$ denotes an offset from the center of $\mathcal{N}_p$. Equal weighting is applied in (2) through mean filtering instead of Gaussian weighting[14,15] to improve computational efficiency. As such, a patch is cuboid instead of an ellipsoid obtianed from Gaussian filtering.[14,15] An asymmetric stencil $\mathcal{N}_s$ depicted in Fig. 1(a) is additionally designed to accentuate structures present along the A-scan direction and minimize sensitivity to poor through-plane resolution.

2. Gradient-based descriptors—gradient information has been shown to capture retinal structures in various successful segmentation algorithms.[16–19] To exploit gradients with neighborhood-based calculation, two classes of descriptors were devised, including AG and CHO. The calculation of AG and CHO involves a patch identical to $\mathcal{N}_p$ and a smaller stencil $\mathcal{N}_{s'}$ used to limit the descriptor dimensionality, providing AG with 18 elements from the average gradients of 6 $\mathcal{N}_p$ for 6 points in $\mathcal{N}_{s'}$. CHO, on the other hand, is built upon AG by populating histograms of 6 orientation bins with an angle θ_k between the average gradient $\boldsymbol{g}_a$ of $\mathcal{N}_p$ and each gradient $\boldsymbol{g}_k$ in $\mathcal{N}_p$ computed using a scalar product

$$\theta_k = \cos^{-1}\left(\frac{\boldsymbol{g}_a \cdot \boldsymbol{g}_k}{\left\|\boldsymbol{g}_a\right\|_2 \left\|\boldsymbol{g}_k\right\|_2}\right). \tag{3}$$

As a result, CHO consists of 6 elements capturing the deviation of $\boldsymbol{g}_k$ from $\boldsymbol{g}_a$ in $\mathcal{N}_p$.

2.2. Symmetric Diffeomorphic Demons Registration

Symmetric diffeomorphic Demons registration[3] seeks a diffeomorphism $\boldsymbol{\phi}_i(\boldsymbol{x}, t) : \Omega \subset \mathbb{R}^3 \times t \in [0, 1] \to \Omega$ which is a flow of time-dependent velocity fields

$$\boldsymbol{\phi}_i(\boldsymbol{x}, t) = \boldsymbol{\phi}_i(\boldsymbol{x}, 0.5) + \int_0^{(-1)^i(0.5-t)} \boldsymbol{v}_i(\boldsymbol{\phi}_i(\boldsymbol{x}, 0.5-(-1)^i\tau), 0.5-(-1)^i\tau)d\tau, \quad i = 0, 1, \tag{4}$$

between a moving image I_0 and a fixed image I_1 such that $I_0 \circ \boldsymbol{\phi}_0 \circ \boldsymbol{\phi}_1^{-1}(z, 0) = I_1(z)$, $\boldsymbol{z} \in \Omega$. The diffeomorphisms $\boldsymbol{\phi}_0(\boldsymbol{x}, t)$ and $\boldsymbol{\phi}_1(\boldsymbol{x}, t)$ are defined for different time points (see Fig. 1 in Reaungamornrat et al.[3]) using a time point variable $t_i = (0.5 - (-1)^i \boldsymbol{\tau}) \in [0, 1]$ defined via pseudo-time $\boldsymbol{\tau} \in [0, 0.5]$. The velocity fields $\boldsymbol{v}_i$ in (4) are defined in the normed space V with a norm $\| \boldsymbol{v}_i(t_i) \|_V = \| L\boldsymbol{v}_i(t_i) \|_2$ and a differential operator $L = (Id + a^2\nabla^2)$ for $a \in \mathbb{R}$. The geodesics of $\boldsymbol{\phi}_i$ are energy minimizing paths with the geodesic shortest length (GSL) measured in terms of the minimizing energy as

$$\rho\left(\boldsymbol{\phi}_i(0.5), \boldsymbol{\phi}_i\right) = \inf_{\boldsymbol{v}_i} \sqrt{\int_0^{0.5} \| \boldsymbol{v}_i(0.5-(-1)^i\tau) \|_V^2 d\tau}, \tag{5}$$

with a boundary $\boldsymbol{\phi}_i(x, 0.5) = \boldsymbol{x}$, $\boldsymbol{\phi}_0(\boldsymbol{x}, 0) = y$, and $\boldsymbol{\phi}_1(\boldsymbol{x}, 1) = \boldsymbol{z}$ for a point $\boldsymbol{x}$, $\boldsymbol{y}$, and $\boldsymbol{z}$ in the domains of a virtual image $I_{0.5}$, I_0, and I_1, respectively. This section briefly summarizes the symmetric diffeomorphic Demons optimization approach used in MIND Demons[3,14] (see prior work[3,14] for detail) and describes extensions added to MIND Demons to enable robust cross-scanner, inter-subject diffeomorphic deformable registration of OCT volumetric images.

1. MIND-Demons optimization—As described in prior work,[3] MIND Demons estimates diffeomorphisms by optimizing the energy functional incorporating priors on invertibility $\boldsymbol{\phi}_i \circ \boldsymbol{\phi}_i^{-1} = Id$ and the equality of GSL $\rho(\boldsymbol{\phi}_0(\boldsymbol{x}, 0.5), \boldsymbol{\phi}_0(\boldsymbol{x})) = \rho(\boldsymbol{\phi}_1(\boldsymbol{x}, 0.5), \boldsymbol{\phi}_1(\boldsymbol{x}))$:

$$\begin{aligned} E\left(\boldsymbol{\phi}_i, \boldsymbol{\eta}_i\right) &= \frac{1}{2}\{\alpha_S^2 \int_{\boldsymbol{x} \in \Omega} H^2\left(I_0 \circ \boldsymbol{\eta}_0, I_1 \circ \boldsymbol{\eta}_1, \boldsymbol{x}\right)d\boldsymbol{x} + \alpha_U^2\left(\rho^2\left(\boldsymbol{\phi}_1^{-1}, \boldsymbol{\eta}_0\right), \rho^2\left(\boldsymbol{\phi}_0^{-1}, \boldsymbol{\eta}_1\right)\right) \\ &+ \alpha_P^2(\| \nabla \boldsymbol{\phi}_1^{-1} \|_2^2 + \| \nabla \boldsymbol{\phi}_0^{-1} \|_2^2)\} \\ &\text{subject to } \boldsymbol{\phi}_i(\boldsymbol{x}, 0.5) = \boldsymbol{\eta}_i(\boldsymbol{x}, 0.5) = Id(\boldsymbol{x}), \rho\left(\boldsymbol{\phi}_0(\boldsymbol{x}, 0.5), \boldsymbol{\phi}_0(\boldsymbol{x})\right) \\ &= \rho\left(\boldsymbol{\phi}_1(\boldsymbol{x}, 0.5), \boldsymbol{\phi}_1(\boldsymbol{x})\right), \text{ and } \boldsymbol{\phi}_i \circ \boldsymbol{\phi}_i^{-1} = Id \end{aligned} \tag{6}$$

where α_S, α_U, and α_P are regularization parameters and $\boldsymbol{\eta}_i = \boldsymbol{\phi}_i\left(Id + L\boldsymbol{v}_i\right) = \boldsymbol{\phi}_j^{-1}\left(Id + L\boldsymbol{v}_i\right)$ are hidden variables representing intermediate diffeomorphisms. The first term in the functional (6) measures similarity between I_0 and I_1 after diffeomorphism using the Huber metric, the second term quantifies the kinetic energy of the diffeomorphisms based on (5), and the last term estimates the harmonic energy of the diffeomorphisms.[3]

Optimization of (6) is performed in two steps.[3] In the first step, the first two terms are minimized under the GSL equality constraint to maximize image alignment using a Gauss-Newton (GN) method. Calculation of GN search directions yields a voxel-wise update field equation:

$$\boldsymbol{u}_i(\boldsymbol{x}) = -\frac{H(\boldsymbol{x})\nabla_i H(\boldsymbol{x})}{\alpha_U^2/\alpha_S^2(\boldsymbol{x}) + \left\|\nabla_i H(\boldsymbol{x})\right\|_2^2} \tag{7}$$

where $\nabla_i H(\boldsymbol{x})$ denotes the gradient of H with respect to $\boldsymbol{\phi}_i$. The update fields are used to increment $\boldsymbol{\eta}_i$ as $\boldsymbol{\eta}_i^k = (\boldsymbol{\phi}_i^{k-1})^{-1} + K(\boldsymbol{u}_i^k)_{L^2} \circ (\boldsymbol{\phi}_j^{k-1})^{-1}$, where k is an iteration number and $K = (L^\dagger L)^{-1}$ is the Green kernel projecting Lagrangian measure-based momentum fields $\boldsymbol{u}_i$ in L^2 (a space of square integrable vector fields) onto V.[3,20–22] In the second step, Tikhonov regularization is applied to estimate smooth diffeomorphisms $\boldsymbol{\phi}_i$ with the priors on the invertibility of $\boldsymbol{\phi}_i$. The optimization method alternates between these two steps until convergence or a maximum number of optimization iterations is reached.

2. D-MIND Demons optimization—In addition to the challenges of image quality that D-MINDs address (described in Section 2.1), acquisition geometry of OCT is typically not properly defined. The fanning of A-scans, for example, is often not acquired and not presented in OCT images but affects the degree of curvature of deformations orthogonal to the A-scan direction.[4] As a result, deformation across different A-scans is difficult to correctly modeled. These additional constraints are added to (6) to permit non-linear alignment only along corresponding A-scans in I_0 and I_1, defined as

$$\left\langle \left(L^\dagger L\right)\boldsymbol{v}_i\left(\boldsymbol{\phi}_i(\boldsymbol{x}, t_i), t_i\right), [1, 1, 0] \right\rangle_{L^2} = 0, \tag{8}$$

where $\langle \cdot, \cdot \rangle_{L^2}$ denotes the inner product in L^2. The constraints force $\boldsymbol{u}_i(\boldsymbol{x}) = (L^\dagger L)\boldsymbol{v}_i(\boldsymbol{\phi}_i(\boldsymbol{x}, t_i), t_i)$ to be parallel to the A-scan direction ($[0,0,1]^T$, corresponding to the z axis of the coordinate system of OCT volumetric data used in this work). Equation (8) can be written in terms of $\boldsymbol{u}_i$ in (7) as $\forall\ \boldsymbol{x} \in \Omega : \langle \boldsymbol{u}_i, [1,1,0] \rangle_{L^2} = 0$, implying that the scalar projection of $\boldsymbol{u}_i$ onto the xy-plane of the coordinate system of OCT is 0 and that $\boldsymbol{u}_i$ are parallel to the A-scan direction or $\mathbf{0}$.

The D-MIND Demons optimization approach is integrated with a multiresolution strategy and convergence criteria (described in prior work[3]) to improve robustness against local minima and ability to resolve large deformation, while preventing excessive optimization iterations. Combinations of descriptors from Section 2.1 (i.e., D-MIND, AG, CHO, COC, and RL) are used as image representations in place of I_0 and I_1, providing D-MIND Demons and its alternatives including D-MIND+CHO, D-MIND+COC+RL, and D-MIND+CHO +COC+RL Demons methods.

3. EXPERIMENTS

3.1. Clinical OCT Data

The performance of descriptors and registration methods were assessed using seven pairs of clinical retina OCT volumetric images in a local institutional review board approved study. For all experiments, I_0 were acquired using a Spectralis OCT system (Heidelberg Engineering, Heidelberg, Germany) with 49 B-scans, each B-scan having 1024 A-scans with 496 voxels per A-scan, and I_1 were acquired using a Cirrus OCT scanner (Carl Zeiss Meditec, Jena, Germany) with 128 B-scans, each B-scan having 512 A-scans with 1024 voxels per A-scan. An OCT voxel size, defined by distances between scan lines, B-mode slices, and A-scan voxels, was approximately 6×125×4 μm^3 for I_0 and 12×47×2 μm^3 for I_1. The coordinate-system convention used here is that B-scan (lateral), slice-separation (through-plane), and A-scan (axial) directions represent the x, y, and z axes, respectively. Shown in Fig. 2 are examples of I_0 and I_1. Each of the first two rows in Fig. 2 shows OCT images acquired from the same patient, while the last row depicts an image pair acquired from different subjects. Separate image pairs were used in the following experiments. Retinal boundaries in all I_0 and I_1 were flattened, as performed in various segmentation algorithms,[16,23,24] by translating all A-scans in each B-scan such that the Bruch's membrane boundary is flat.[16] I_0 and I_1 were initially aligned using a NMI registration method with a fovea-position constraint. For target point definition (TRE calculation), retina layers in I_0 and I_1 were segmented and points along the boundaries of the layers were used as target points.[16] The corresponding target points in I_0 and I_1 with TRE after rigid registration < 1μm were referred to as *matched points* (~94,000 points).

3.1. Analysis of Effects of Denoising Methods on Feature Performance

The effect of BM3D[5] and FNLM[6] denoising on the ability of descriptors to discriminate distinct local structure/texture was investigated using two pairs of OCT images, each acquired from the same patient. The ability of descriptors $\boldsymbol{d}_i$ and $\boldsymbol{d}_j$ in images I_i and I_j was quantified using mutual descriptiveness,

$$\mathrm{MD}\left(\boldsymbol{d}_i, \boldsymbol{d}_j, \boldsymbol{x}, \mathcal{N}_q\right) = \frac{U_i\left(\boldsymbol{d}_i, \boldsymbol{d}_j, \boldsymbol{x}, \mathcal{N}_q\right) + U_j\left(\boldsymbol{d}_j, \boldsymbol{d}_i, \boldsymbol{x}, \mathcal{N}_q\right)}{2 + 2H\left(\boldsymbol{d}_i(\boldsymbol{x}), \boldsymbol{d}_j(\boldsymbol{x})\right)} \in [0, 1] \tag{9}$$

combining the Huber dissimilarity measure H and the uniqueness U_i determined by the similarity of a descriptor to its neighboring descriptors defined in a neighborhood $\mathcal{N}_q$ in I_i and I_j as

$$\begin{aligned} U_i\left(\boldsymbol{d}_i, \boldsymbol{d}_j, \boldsymbol{x}, \mathcal{N}_q\right) = \frac{1}{2\left|\mathcal{N}_q\right|} \sum_{\boldsymbol{q} \in \mathcal{N}_q} \sum_{k=1}^{D} \frac{\left|\log\left(d_{i,k}(\boldsymbol{x})/d_{i,k}(\boldsymbol{x}+\boldsymbol{q})\right)\right|}{1 + \left|\log\left(d_{i,k}(\boldsymbol{x})/d_{i,k}(\boldsymbol{x}+\boldsymbol{q})\right)\right|} \\ + \frac{\left|\log\left(d_{i,k}(\boldsymbol{x})/d_{j,k}(\boldsymbol{x}+\boldsymbol{q})\right)\right|}{1 + \left|\log\left(d_{i,k}(\boldsymbol{x})/d_{j,k}(\boldsymbol{x}+\boldsymbol{q})\right)\right|} \in [0, 1] \end{aligned} \tag{10}$$

where $\boldsymbol{q}$ is an offset from the center of $\mathcal{N}_q$. The uniqueness U_j is computed similarly.

Equation (10) was inspired by the measure of uniqueness of an image neighborhood described in previous work;[25] U_i, however, is distinct since it measures the uniqueness of an individual descriptor $\boldsymbol{d}_i$ (not a neighborhood) compared to descriptors in its neighborhood and the corresponding neighborhood in another image. MD in (9), as a result, quantifies not only the uniqueness of two corresponding descriptors $\boldsymbol{d}_i$ and $\boldsymbol{d}_j$ but also the similarity between them. The more similar the corresponding descriptors and the more unique the descriptors from their neighboring descriptors, the better the descriptor ability to uniquely represent local structure/texture and the higher the value of MD.

3.2 Ranking of Descriptor Performance

Elements of descriptors (described in Section 2.1) were ranked according to the difference between the median of MD computed at match points and that computed at points in homogenous regions. This difference demonstrates the ability to capture local information while faithfully representing homogenous regions. Ranking was performed using two OCT pairs (distinct from those used in Section 3.1), each acquired from the same subject, before and after denoising. The descriptor elements with high ranking formed descriptors (image representations) incorporated in Demons-based registration methods described in Section 2.2.

3.3 Analysis of Descriptor Performance in Demons

The combination of descriptor elements that yielded the best registration performance were identified using three OCT image pairs (Fig. 2). As Section 4.2 shows elements of D-MIND, CHO, COC, and RL achieved high rank, the registration approaches investigated included D-MIND, D-MIND+CHO, D-MIND+COC+RL, and D-MIND+CHO+COC+RL Demons methods. Two image pairs—each acquired from the same patient—were well aligned after NMI rigid registration (TRE = 4±6 μm) and used to investigate the reliability and stability of each Demons variant. The most stable and reliable method with the best computational efficiency was identified as a nominal method, and was evaluated in inter-scanner, inter-subject deformable image registration.

4. RESULTS

4.1. Effects of Denoising Methods on Feature Performance

Figure 3 demonstrates the effect of B3MD and FNLM on descriptiveness of features at match points (filled markers) and points in homogenous regions (hollow markers). The plots show the median of MD of descriptor elements computed on images before and after BM3D and FNLM denoising. Element numbers and their meaning are described in Fig.1. BM3D yielded statistically significant improvement (p-value << 0.001) in MD at match points for D-MIND and AG, while FNLM statistically significantly improved MD of COC and RL (p-value << 0.001). The benefit of denoising to CHO, however, was not observed. Regardless of denoising methods, D-MINDs demonstrated the best ability to faithfully represent homogenous regions (Fig. 3).

4.2 Ranking of Descriptor Performance

Figure 4 summarizes the ranking of descriptor elements of images before and after BM3D and FNML denoising. An element achieving the highest difference in the median mutual descriptiveness measured in high-contrast and homogenous regions is depicted in the top left corner, and one with the lowest difference is shown in the bottom right corner. The top 28 ranks were considered high ranks. Regardless of denoising methods, D-MIND elements, except numbers 1 and 7, occupied high ranks. AG, on the other hand, earned low ranks, and was omitted from further study. Some elements of CHO (#2–#6), COC (#1, #3, and #4), and RL (#9, #7, and #5) achieved high ranks. The high-ranking elements were combined, giving Demons variants investigated in the following experiment.

4.3 Descriptor Performance in Demons

Figure 5 summarizes the performance of each Demons variant in intra-subject registration of rigidly well-aligned OCT pairs. CHO showed sensitivity to noise, introducing misalignment between noisy images. D-MIND Demons and the others, however, maintained, if not improved, TRE, demonstrating stability. As denoising and addition of other descriptors increased computation time, D-MIND Demons without denoising methods was a nominal registration approach. The performance of D-MIND Demons in inter-scanner, inter-subject registration is summarized in Fig. 6. Figures 6(a–c) show D-MIND Demons improved image alignment from TRE = 12±8 μm to 4±6 μm. The estimated deformation was additionally diffeomorphic with invertibility error[3] of 0.005±0.007 μm and minimum of Jacobian determinant[3] of 0.17 as captured in Fig. 6(d).

5. DISCUSSION and CONCLUSIONS

A deformable registration method estimating diffeomorphisms between retinal OCT volumetric images has been developed by incorporating D-MINDs, which reduces sensitivity to intensity non-uniformity, minimizes effects of central-patch degradation, uses the Huber metric to improve robustness against noise and speckle, and employs an asymmetric stencil to accommodate poor through-plane resolution. The method constrains the direction of velocity fields to be parallel to that of A-scans. Among descriptors investigated, D-MINDs demonstrated the superior ability to distinguish local structures while faithfully capturing homogenous regions. Validation of the D-MIND Demons method in cross-scanner OCT registration showed the method outperformed the other variants with better computational efficiency, robustness against typical degradation of OCT images, and accuracy (4 μm) comparable to, if not better than, voxel size. Future work includes analysis in a larger dataset and application to longitudinal evaluation of anatomical changes, population-based studies, and image segmentation.

ACKNOWLEDGMENTS

This work was supported in part by the National Institutes of Health grant number 5R01EY024655. The authors gratefully acknowledge Dr. Jeffrey H. Siewerdsen (Biomedical Engineering, Johns Hopkins University) for a discussion on the MIND Demons algorithm.

REFERENCES

[1]. Gordon-Lipkin E, Chodkowski B, Reich DS, Smith SA, Pulicken M, Balcer LJ, Frohman EM, Cutter G and Calabresi PA, "Retinal nerve fiber layer is associated with brain atrophy in multiple sclerosis," Neurology 69(16), 1603–1609 (2007). [PubMed: 17938370]

[2]. Lu Y, Li Z, Zhang X, Ming B, Jia J, Wang R and Ma D, "Retinal nerve fiber layer structure abnormalities in early Alzheimer's disease: Evidence in optical coherence tomography," Neurosci. Lett 480(1), 69–72 (2010). [PubMed: 20609426]

[3]. Reaungamornrat S, De Silva T, Uneri A, Vogt S, Kleinszig G, Khanna AJ, Wolinsky J-P, Prince JL and Siewerdsen JH, "MIND Demons: Symmetric Diffeomorphic Deformable Registration of MR and CT for Image-Guided Spine Surgery," IEEE Trans. Med. Imaging 35(11), 2413–2424 (2016). [PubMed: 27295656]

[4]. Chen M, Lang A, Ying HS, Calabresi PA, Prince JL and Carass A, "Analysis of macular OCT images using deformable registration.," Biomed. Opt. Express 5(7), 2196–2214 (2014). [PubMed: 25071959]

[5]. Danielyan A, Katkovnik V and Egiazarian K, "BM3D Frames and Variational Image Deblurring," IEEE Trans. Image Process 21(4), 1715–1728 (2012). [PubMed: 22128008]

[6]. Foi A and Boracchi G, "Foveated Nonlocal Self-Similarity," Int. J. Comput. Vis 120(1), 78–110 (2016).

[7]. Haralick RM, Shanmugam K and Dinstein I, "Textural Features for Image Classification," IEEE Trans. Syst. Man. Cybern SMC-3(6), 610–621 (1973).

[8]. Dasarathy BV and Holder EB, "Image characterizations based on joint gray level—run length distributions," Pattern Recognit. Lett 12(8), 497–502 (1991).

[9]. Myronenko A and Xubo Song., "Intensity-Based Image Registration by Minimizing Residual Complexity," IEEE Trans. Med. Imaging 29(11), 1882–1891 (2010). [PubMed: 20562036]

[10]. Fuerst B, Wein W and Müller M, "Automatic ultrasound–MRI registration for neurosurgery using the 2D and 3D LC2 Metric," Med. Image Anal 18(8), 1312–1319 (2014). [PubMed: 24842859]

[11]. Wang F and Vemuri BC, "Non-Rigid Multi-Modal Image Registration Using Cross-Cumulative Residual Entropy," Int. J. Comput. Vis 74(2), 201–215 (2007). [PubMed: 20717477]

[12]. Heinrich MP, Jenkinson M, Bhushan M, Matin T, Gleeson FV, Brady SM and Schnabel JA, "MIND: Modality independent neighbourhood descriptor for multi-modal deformable registration," Med. Image Anal 16(7), 1423–1435 (2012). [PubMed: 22722056]

[13]. Huber PJ, "Robust Regression: Asymptotics, Conjectures and Monte Carlo," Ann. Stat 1(5), 799–821 (1973).

[14]. Reaungamornrat S, De Silva T, Uneri A, Wolinsky J-P, Khanna AJ, Kleinszig G, Vogt S, Prince JL and Siewerdsen JH, "MIND Demons for MR-to-CT deformable image registration in image-guided spine surgery," SPIE Med. Imaging, Webster RJ and Yaniv ZR, Eds., 97860H, International Society for Optics and Photonics (2016).

[15]. Reaungamornrat S, De Silva T, Uneri A, Goerres J, Jacobson M, Ketcha M, Vogt S, Kleinszig G, Khanna AJ, Wolinsky J-P, Prince JL and Siewerdsen JH, "Performance evaluation of MIND demons deformable registration of MR and CT images in spinal interventions," Phys. Med. Biol 61(23), 8276–8297 (2016). [PubMed: 27811396]

[16]. Lang A, Carass A, Hauser M, Sotirchos ES, Calabresi PA, Ying HS and Prince JL, "Retinal layer segmentation of macular OCT images using boundary classification.," Biomed. Opt. Express 4(7), 1133–1152 (2013). [PubMed: 23847738]

[17]. Carass A, Lang A, Hauser M, Calabresi PA, Ying HS and Prince JL, "Multiple-object geometric deformable model for segmentation of macular OCT.," Biomed. Opt. Express 5(4), 1062–1074 (2014). [PubMed: 24761289]

[18]. Yazdanpanah A, Hamarneh G, Smith B and Sarunic M, "Intra-retinal Layer Segmentation in Optical Coherence Tomography Using an Active Contour Approach," Springer, Berlin, Heidelberg, 649–656 (2009).

[19]. Kafieh R, Rabbani H and Kermani S, "A review of algorithms for segmentation of optical coherence tomography from retina.," J. Med. Signals Sens 3(1), 45–60 (2013). [PubMed: 24083137]

[20]. Miller MI, Trouvé A and Younes L, "Geodesic Shooting for Computational Anatomy.," J. Math. Imaging Vis 24(2), 209–228 (2006). [PubMed: 20613972]

[21]. Avants BB, Epstein CL, Grossman M and Gee JC, "Symmetric diffeomorphic image registration with cross-correlation: evaluating automated labeling of elderly and neurodegenerative brain," Med. iImage Anal 12(1), 2007/7/31, 26–41 (2008).

[22]. Wang L, Beg F, Ratnanather T, Ceritoglu C, Younes L, Morris JC, Csernansky JG and Miller MI, "Large Deformation Diffeomorphism and Momentum Based Hippocampal Shape Discrimination in Dementia of the Alzheimer type," IEEE Trans. Med. Imaging 26(4), 462–470 (2007). [PubMed: 17427733]

[23]. Garvin MK, Abramoff MD, Xiaodong Wu, Russell SR, Burns TL and Sonka M, "Automated 3-D Intraretinal Layer Segmentation of Macular Spectral-Domain Optical Coherence Tomography Images," IEEE Trans. Med. Imaging 28(9), 1436–1447 (2009). [PubMed: 19278927]

[24]. Chiu SJ, Li XT, Nicholas P, Toth CA, Izatt JA and Farsiu S, "Automatic segmentation of seven retinal layers in SDOCT images congruent with expert manual segmentation," Opt. Express 18(18), 19413 (2010). [PubMed: 20940837]

[25]. Goshtasby AA, "Point Detectors," 67–121 (2012).

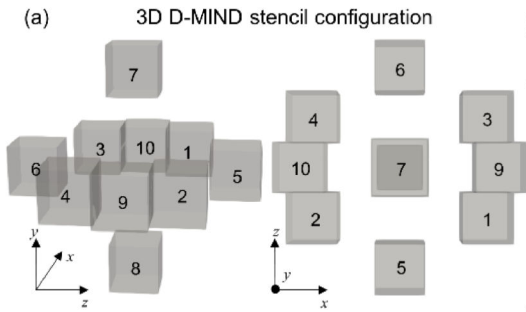

(b) D-MIND element numbers

Element Number	Patch Pairs	Element Number	Patch Pairs
1	(1,2)	8	(4,6)
2	(1,5)	9	(5,6)
3	(1,4)	10	(7,5)
4	(2,5)	11	(7,6)
5	(2,3)	12	(7,8)
6	(3,6)	13	(8,9)
7	(3,4)	14	(9,10)

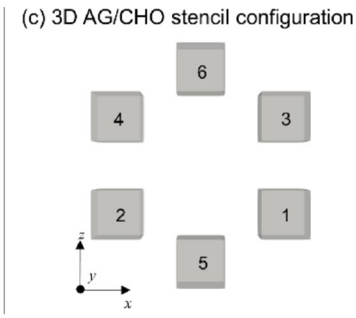

Figure 1.

3D stencil configurations of D-MIND, AG, and CHO descriptors. (a) D-MIND stencil configuration with 14 elements computed from patch distances between (b) patch pairs. A cuboid depicts a patch whose size and shape are determined by offsets and weights in (2), e.g., an ellipsoidal patch can be approximated using Gaussian weights. The numbers on the cuboids denote the indices of points in the stencil, used to defined (b) patch pairs. (c) AG and CHO stencil configuration with a smaller number of elements to reduce the descriptor dimensionality. The x, y, and z axes represent the B-scan (lateral), through-B-mode-plane, and A-scan (axial) directions, respectively.

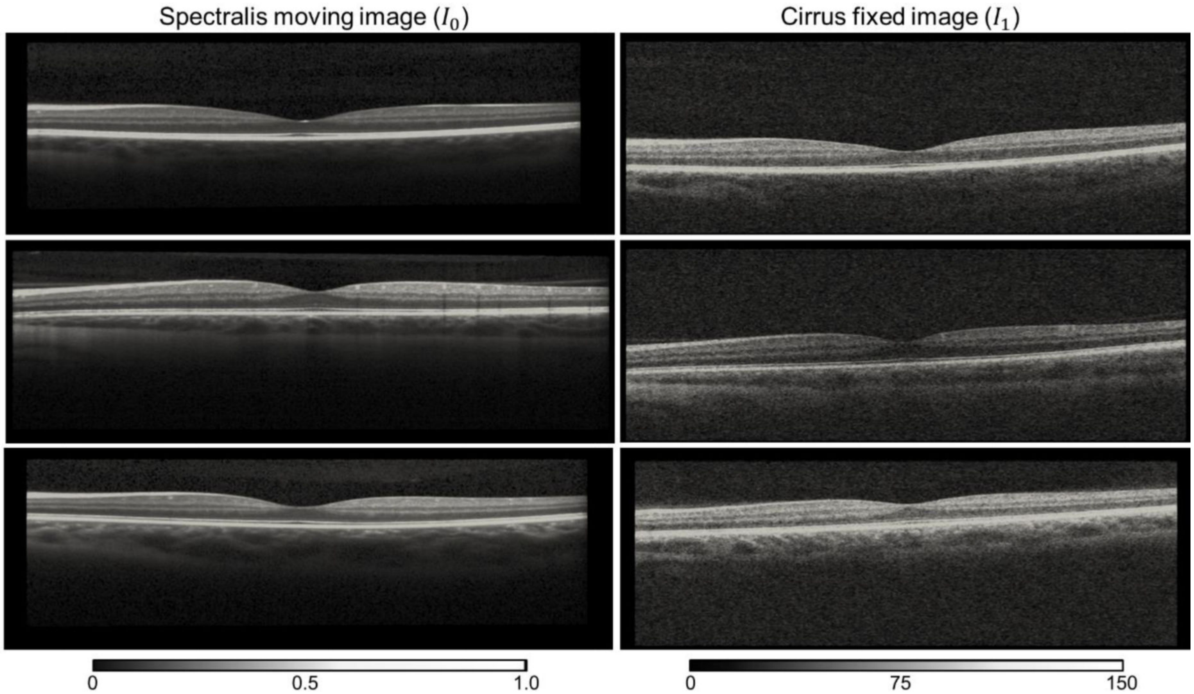

Figure 2.

Example retina OCT images acquired using (left) Spectralis and (right) Cirrus OCT imaging systems. A pair of I_0 and I_1 on the first two rows were each acquired from the same patient. I_0 and I_1 on the last row were acquired from different patients for inter-scanner, inter-subject evaluation.

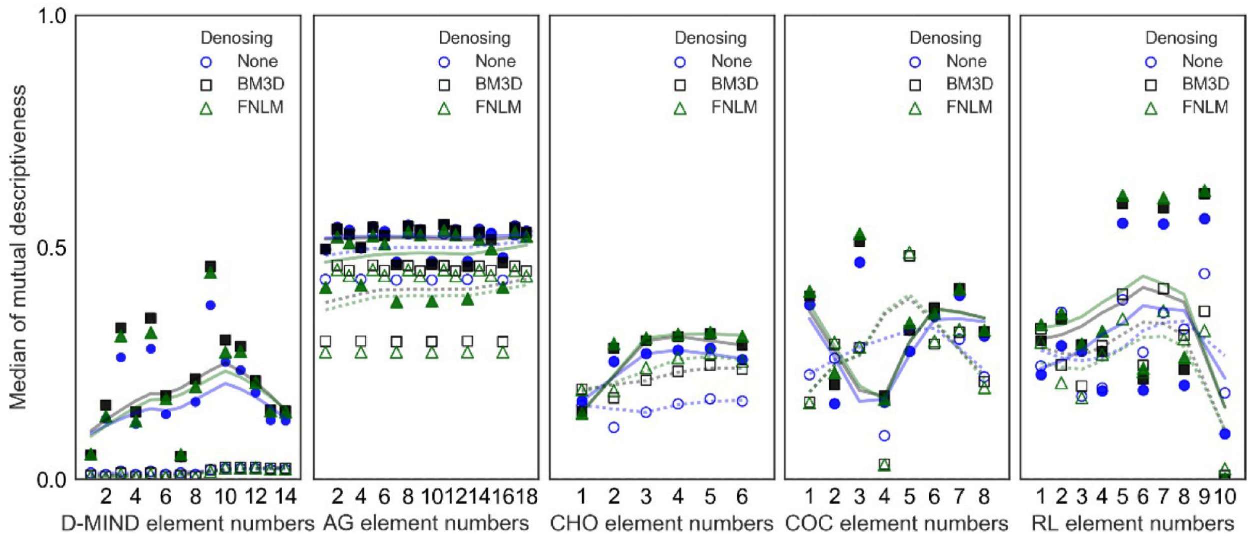

Figure 3.

Effect of denoising on mutual descriptiveness of descriptor elements at match points (filled marker) and points in homogenous regions (hollow markers). From left to right, median mutual descriptiveness for descriptor elements of D-MINDs, average image gradients, compact histograms of image orientation, co-occurrence texture features, and run-length texture features. The blue circles, black squares, and green triangles mark the median mutual descriptiveness for no filtering, BM3D, and FNLM, respectively. Solid and dot lines are linear fits for measures of match points and points in homogenous regions.

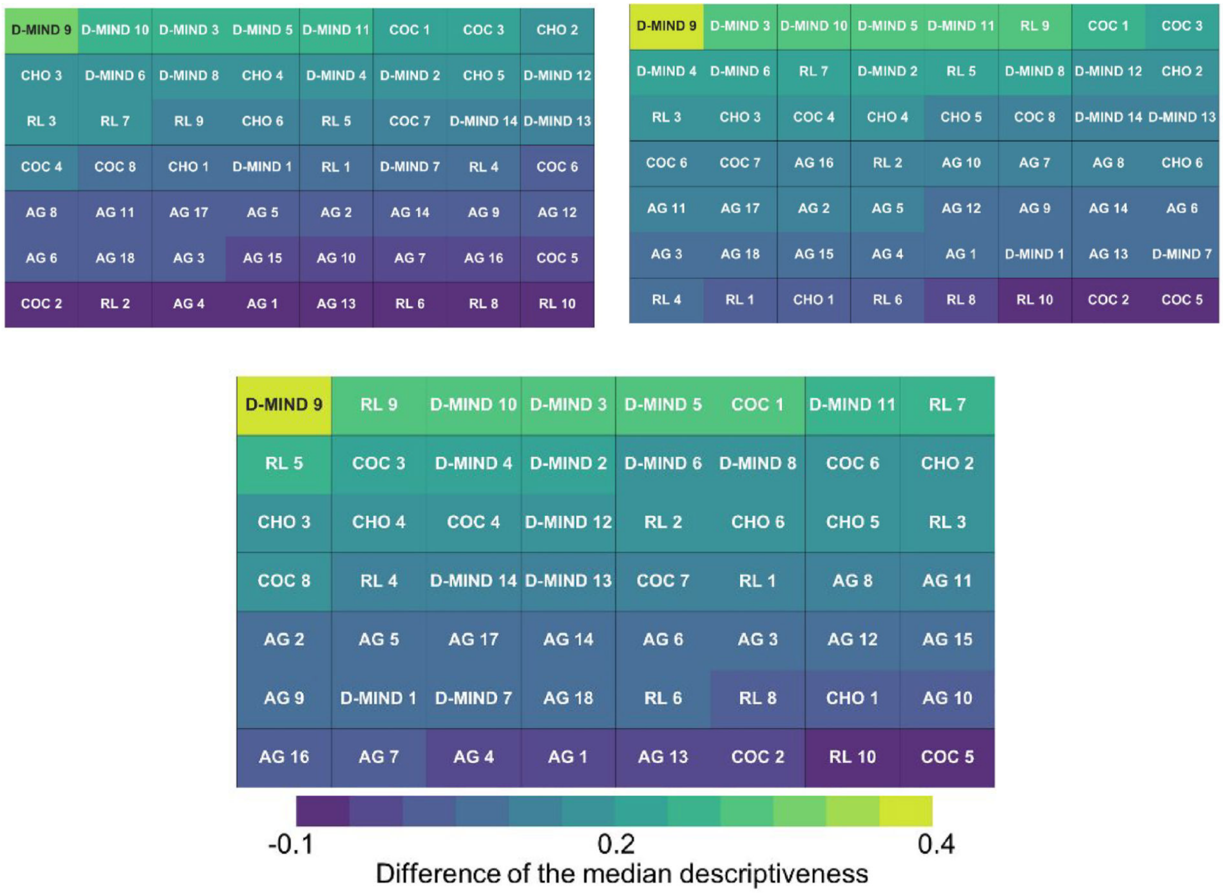

Figure 4.

Ranking of descriptor elements according to the difference between the median mutual descriptiveness of the elements measured at match points and that measured at points in homogenous regions. (Top) from left to right, descriptors were computed on images before and after BM3D denoising, respectively. (Bottom) descriptors were computed on images after FNLM denoising. The maps are colored according to the difference in the median mutual descriptiveness.

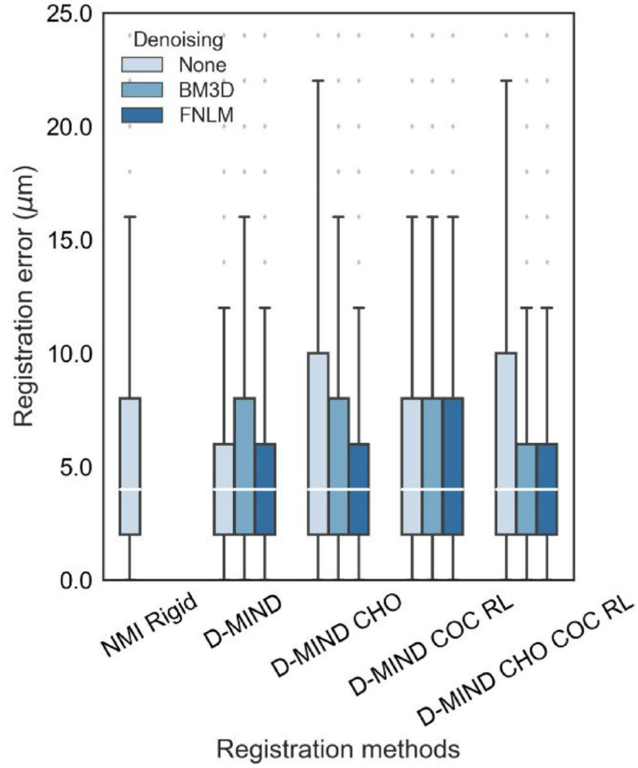

Figure 5.

TRE measured for cross-scanner intra-subject diffeomorphic deformable registration of OCT images before and after BM3D and FNLM denoising using NMI rigid registration and variants of the D-MIND Demons method, including D-MIND+CHO, D-MIND+COC+RL, D-MIND+CHO+COC+RL Demons registrations.

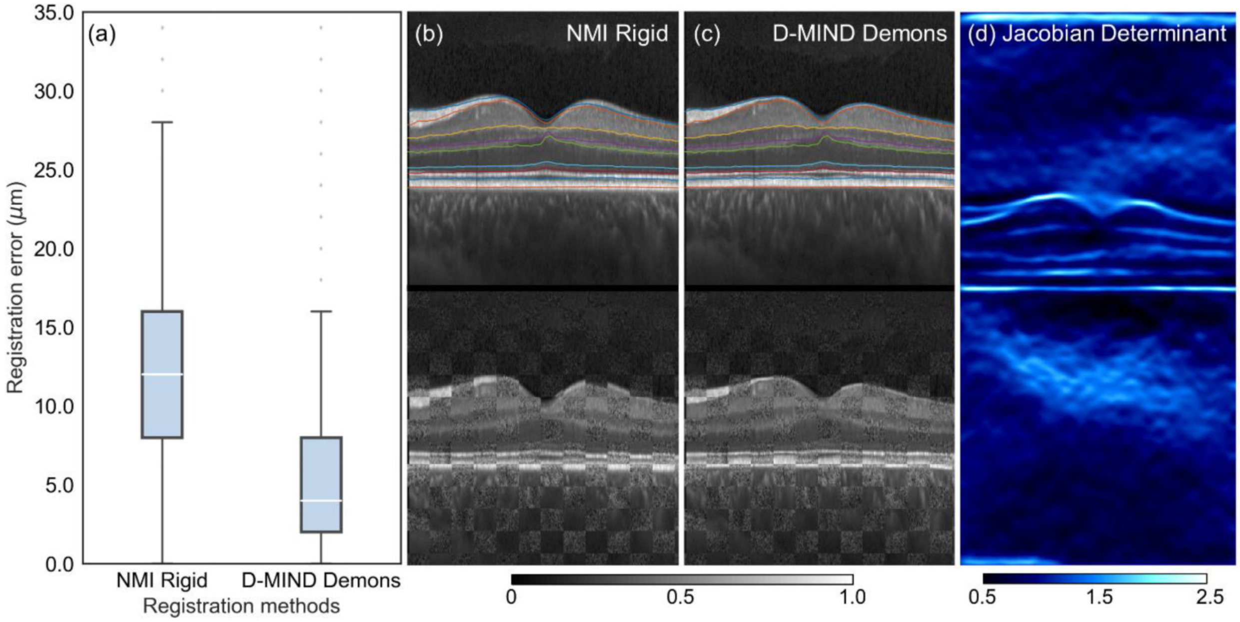

Figure 6.

Cross-scanner inter-subject diffeomorphic deformable OCT registration using D-MIND Demons. (a) TRE resulting from NMI rigid and D-MIND Demons registration. (b) Superposition of retinal layer contours in I_1 on I_0 after NMI rigid registration (top) and a checkerboard image of I_1 and I_0 after rigid registration (bottom). (c) The same, for D-MIND Demons registration. (d) Jacobian determinants of the estimated deformation.